

Long-term Stable Nonlinear Evolutions of Ultracompact Black-Hole Mimickers

Gareth Arturo Marks ^{1,*} Seppe J. Staelens ^{2,3,†} Tamara Evstafyeva ^{4,‡} and Ulrich Sperhake ^{2,5,6,§}

¹*DAMTP, Centre for Mathematical Sciences, University of Cambridge,
Wilberforce Road, Cambridge CB3 0WA, United Kingdom*

²*DAMTP, Centre for Mathematical Sciences, University of Cambridge, Wilberforce Road, Cambridge CB3 0WA, UK*

³*Leuven Gravity Institute, KU Leuven, Celestijnenlaan 200D box 2415, 3001 Leuven, Belgium*

⁴*Perimeter Institute for Theoretical Physics, Waterloo, Ontario N2L 2Y5, Canada*

⁵*Department of Physics and Astronomy, Johns Hopkins University,
3400 North Charles Street, Baltimore, Maryland 21218, USA*

⁶*TAPIR 350-17, Caltech, 1200 E. California Boulevard, Pasadena, California 91125, USA*

(Dated: September 17, 2025)

We study the stability of ultracompact boson stars admitting light rings combining a perturbative analysis with 3+1 numerical-relativity simulations with and without symmetry assumptions. We observe excellent agreement between all perturbative and numerical results which uniformly support the hypothesis that this family of black-hole mimickers is separated into stable and unstable branches by extremal-mass configurations. This separation includes, in particular, thin-shell boson stars with light rings located on the stable branch which we conclude to represent long-term stable black-hole mimickers.

Introduction—Black-hole solutions in closed analytic form have played a crucial role in many aspects of the theoretical understanding of general relativity (GR) almost right from the moment Einstein published his theory. Starting with observations of X-ray sources (e.g. Cygnus X-1 [1]) and quasars (e.g. 3C 273 [2, 3]) and their eventual identification with accretion onto compact objects, black holes (BHs) acquired an equally prominent role as seemingly common citizens of our Universe. The rapidly increasing number of gravitational-wave (GW) detections by LIGO and Virgo [4, 5], all compatible with theoretical predictions for BHs and neutron stars in GR [6], and direct observations of BH environments by the Event Horizon Telescope [7, 8] have further cemented the prominence of BHs in observational astronomy.

In both mathematical modeling as well as popular imagination, the most characteristic feature of a BH is its event horizon, the 2+1 dimensional outer boundary of the set of spacetime points from which no null geodesics can reach future null infinity. In terms of their observational phenomenology, however, the decisive feature of BHs is their (unstable) light rings (LRs), circular null geodesics on which photons can orbit; for a Schwarzschild BH of mass M , the event horizon is located at areal radius $r = 2GM/c^2$ and the LR at $r = 3GM/c^2$. The appearance of accreting BHs is strongly influenced by the presence and properties of the LR, while quasinormal modes have been shown to have a close connection with null unstable geodesics [9–14]. The observational evidence therefore points more directly at the existence of LRs, not necessarily BHs. Additionally, classical black holes come with theoretical issues, like the singularity

problem [15] or the information paradox [16], motivating the study of BH mimickers. Even if one accepts Occam’s razor and parsimoniously interprets BHs as the most likely sources, there remains the intriguing possibility that a population of ultracompact objects (UCOs) is hiding inside a more conventional BH society and may provide us with clues about the dark-matter candidate fields they are composed of. We also note that the GW emission from compact boson-star (BS) binaries exhibits significant degeneracy with that from BH binaries [17].

Clearly, dynamical longevity is a key requirement of any viable alternative to the BH paradigm. The stability of UCOs or *BH mimickers* – both implied henceforth to denote objects with a LR but no horizon – has, consequently, gained much attention in recent years. Under a broad set of assumptions, BH mimickers have been shown to possess two LRs, one stable and one unstable located at the minimum and maximum, respectively, of the null geodesic’s potential [18, 19]; Kerr BHs, in contrast have unstable LRs only. The existence of a minimum in the effective potential leads to *stable trapping*, i.e. null geodesics originating close to the minimum may remain indefinitely bound to it. At linear level, waves propagating on a background spacetime with stable trapping exhibit decay slower than polynomial or exponential as occurs for unstable trapping [20]. Guided by results on the instability of anti-de Sitter spacetime and its similar decay rates [21–23], it has been heuristically argued that UCOs may also be nonlinearly unstable, thus ruling them out as plausible BH mimickers [24]. In the absence of rigorous analytic results, however, numerical evolutions are the only available tool for testing this hypothesis.

To date, literature results investigating the ultimate fate and stability of UCOs are inconclusive. By simulating two families of ultracompact BSs, Ref. [25] finds either migration to nonultracompact configurations or collapse to a BH, typically on timescales $\lesssim \mathcal{O}(10^3) \mu^{-1}$ in units of the scalar mass parameter, and concludes that

* gam54@cam.ac.uk

† ss3033@cam.ac.uk

‡ tevstafyeva@perimeterinstitute.ca

§ U.Sperhake@damtp.cam.ac.uk

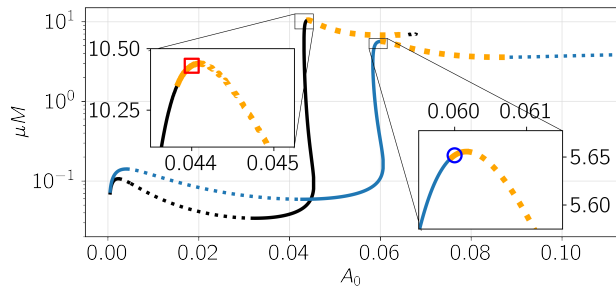


FIG. 1. The ADM mass is shown versus the central scalar-field amplitude A_0 for the one-parameter families of BS models with solitonic potential parameter $\sigma_0 = 0.06$ (black) and $\sigma_0 = 0.08$ (blue). For each family, solid (dashed) segments mark perturbatively stable (unstable) branches and we highlight in orange color BSs exhibiting a pair of LR. The insets indicate the two perturbatively stable BH mimickers with parameters detailed in Table I that form the focus of our numerical investigation.

the LR trigger instability. Reference [26] explains the instability as the result of the backreaction of perturbations at the stable LR appearing to deepen the geodesic potential. In contrast, simulations of the merger and ring-down of ultracompact spinning BSs yield no evidence of this instability [27], although the timescales the simulations span in that work are considerably shorter. Further simulations in spherical symmetry of scalarized Reissner-Nordström BHs with LR also exhibited long-term stability [28]. In a recent study using a toy-model spacetime with two LR, Ref. [29] analyzes the differences between linear and nonlinear dynamics in more detail: within the region of stable trapping, the slow linear decay leads to a growth of higher-order derivatives and energy in the nonlinear evolution, thereby resulting in turbulent behaviour. This phenomenon is proven in the perturbative regime [30], where the authors argue how it may not necessarily trigger an instability. The ultimate end state of these configurations, however, remains an open question.

Here, we explore the stability of a class of spherically symmetric ultracompact BSs with LR characterized by *thin-shell* profiles [31] and reaching compactness $C \sim 0.32$. We combine a set of numerical simulations in spherical symmetry (1+1), axisymmetry (2+1), and full 3+1 dimensions with perturbative calculations of the radial oscillation frequency, observing excellent agreement between all approaches compatible with the standard result that stable and unstable branches of stars, including UCOs with LR, are separated by local extrema in the mass-radius diagram. In particular, we observe no signs of instability on the stable branch containing BH mimickers, in agreement with the restabilization, i.e. real frequency, of the fundamental radial oscillation mode predicted in this regime by our perturbative calculations. Henceforth, we employ Planck units $c = G = \hbar = 1$ but keep the scalar-field mass parameter μ which controls the

TABLE I. Nickname, solitonic parameter σ_0 , central scalar-field amplitude A_0 , ADM mass M , Noether charge \mathcal{N} , the radius r_{99} encompassing 99% of the total mass, compactness $C := M/r_{99}$ and fundamental radial oscillation frequency χ_0^2 for the two BS models marked by square and circle in Fig. 1.

Model	σ_0	A_0	μM	$\mu^2 \mathcal{N}$	μr_{99}	C	χ_0^2/μ^2
S06A044	0.06	0.044	10.43	65.9	31.7	0.33	7.52×10^{-5}
S08A06	0.08	0.06	5.65	26.1	17.9	0.31	2.68×10^{-5}

scale invariance of the spacetimes in question. Code units are translated into SI (or similar) by fixing μ and scaling with appropriate powers thereof: e.g. $\mu = 1.33 \times 10^{-10}$ eV corresponds to $\mu^{-1} = M_\odot = 1.48$ km.

Theory and numerical codes—We consider BSs in GR composed of one minimally coupled, complex scalar field φ , with solitonic potential, described by the action

$$S = \int \sqrt{-g} \left\{ \frac{R}{16\pi} - \frac{1}{2} [g^{\mu\nu} \nabla_\mu \bar{\varphi} \nabla_\nu \varphi + V(\varphi)] \right\} d^4x,$$

$$V(\varphi) = \mu^2 |\varphi|^2 \left(1 - 2 \frac{|\varphi|^2}{\sigma_0^2} \right)^2, \quad \sigma_0 = \text{const.} \quad (1)$$

Varying S results in the Einstein-Klein-Gordon equations

$$G_{\alpha\beta} = 8\pi T_{\alpha\beta}, \quad \nabla^\mu \nabla_\mu \varphi = \frac{dV}{d\varphi}, \quad (2)$$

$$T_{\mu\nu} = \frac{1}{2} \nabla_\nu (\mu \bar{\varphi} \nabla_\nu \varphi) - \frac{g_{\mu\nu}}{2} [g^{\alpha\beta} \nabla_\alpha \bar{\varphi} \nabla_\beta \varphi + V(\varphi)].$$

We compute stationary BS models in spherical symmetry writing $\varphi(t, r) = A(r)e^{i\omega t}$ and using a GR version with quadruple precision of the two-way shooting code of Ref. [32]. The resulting single-BS spacetimes are evolved in time using four different codes in spherical symmetry, axisymmetry, or full 3D using the Baumgarte-Shapiro-Shibata-Nakamura (BSSN) [33, 34] and the conformal covariant Z_4 (CCZ4) [35] formulations. (i) SPHERICALBS-EVOLVER achieves spherically symmetric time evolutions through dimensional reduction with $SO(3)$ symmetry according to Ref. [36] using a uniform radial grid. (ii) A 2D code implements axisymmetry using the same modified cartoon method but for $SO(2)$ isometry. It is based on (iii) EXOZVEZDA [37], a code for exotic matter built on GRCHOMBO [38, 39], which evolves 3D domains with adaptive mesh refinement provided by CHOMBO [40]. (iv) LEAN [41] is based on the CACTUS computational toolkit [42] and evolves 3D domains with mesh refinement provided by CARPET [43]. We will refer to these codes and their respective simulations with the acronyms Sph, Axi, E3D and L3D. Unless specified otherwise, our simulations employ 4th-order discretization, a resolution $h = 1/(12\mu)$ with outer boundary at $256 \mu^{-1}$ on a unigrid (Sph) or using 5 refinement levels (Axi, E3D, L3D).

Time evolutions—Our study focuses on BS families for two values of the solitonic parameter, $\sigma_0 = 0.08$ and $\sigma_0 = 0.06$; the resulting BS models are displayed in the plane spanned by the central scalar amplitude A_0 and the

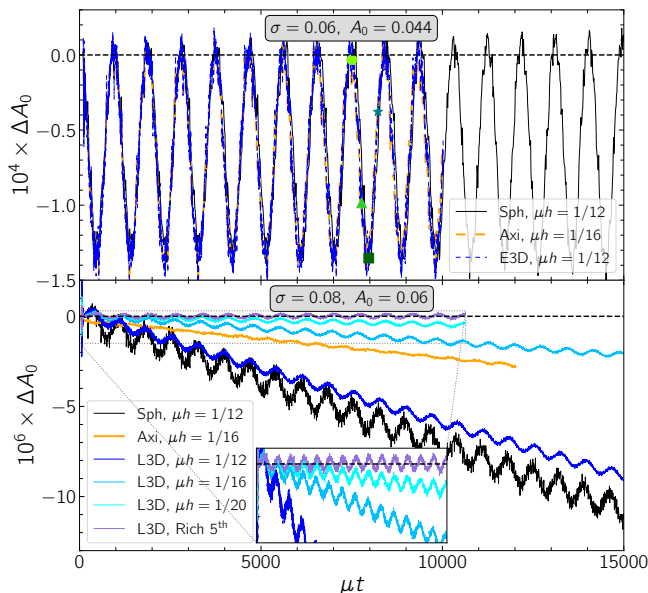


FIG. 2. Time evolution of the deviation ΔA_0 of the central scalar-field amplitude for the S06A044 (top) and S08A06 (bottom) models obtained in spherical symmetry, axisymmetry and 3D. The linear drift visible for S08A06 converges away as shown in the inset. The four symbols in the top panel mark times when we evaluate the LR potential; cf. Fig. 4.

Arnowitt-Deser-Misner (ADM) mass M in Fig. 1. There, we mark in orange color the ultracompact BSs possessing a pair of LRs; for both σ_0 values, this set of UCOs extends to the left, beyond the global maximum of the $M(A_0)$ curve, i.e. into the radially stable branch. This regime comprises the stars of interest in our study and we mark for each potential one representative specimen with properties as summarized in Table I.

We begin our assessment of these two models by plotting in Fig. 2 the deviation ΔA_0 of the central scalar-field amplitude from its initial value over time as obtained with different symmetry assumptions. For the S06A044 model, we observe periodic oscillations with a relative magnitude $\sim 0.3\%$ and good agreement by all codes. For S08A06, the oscillations are 2 orders of magnitude smaller and exhibit a linear drift which converges away with increasing resolution. This is demonstrated by the three blue-shaded curves obtained with L3D using different grid spacing h . Closer analysis of the differences yields 5th-order convergence and the Richardson extrapolated function oscillates with high precision around zero.

Two features manifest in this figure require further explanation. First, we attribute the considerably larger oscillations observed for S06A044 to a larger numerical error in the initial data; for this model, round-off uncertainty in the BS frequency $\sim 10^{-32}$ can effect relative variations in the ADM mass or central lapse comparable to the level $\Delta A_0/A_0$ observed. The S08A06 model is less challenging and results in initial data with small uncertainty compared to those incurred in the time evo-

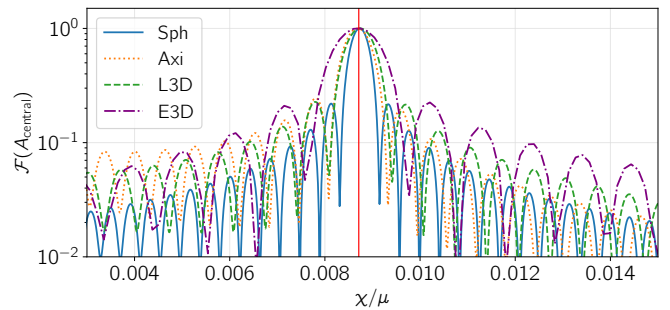


FIG. 3. Power spectrum of $\Delta A_0(t)$ for S08A060; the red line marks the fundamental radial mode frequency χ_0 . Units on the vertical axis are arbitrary.

lutions. This feature also explains the level of agreement between time evolutions employing different symmetry: the perturbations of S06A044 are initial-data dominated with comparatively smaller contributions from the time evolution. For S08A06, on the other hand, details of the time evolution dominate, resulting in more pronounced relative – albeit tiny absolute – differences. This observation is confirmed by artificially lowering the quality of the initial data or time evolution which amplifies drift or oscillation magnitude but with no change in frequency. The 3D simulations displayed here have been computed using octant symmetry. We have performed additional versions of the 3D simulations of S08A06 using L3D (E3D) with $h = 1/12$ in full grid mode up to $t \gtrsim 3000$ ($t \gtrsim 1000$); these give identical results to the octant runs within round-off precision.

The time evolution of the maximal Kretschmann scalar $R^{\alpha\beta\gamma\delta}R_{\alpha\beta\gamma\delta}$ exhibits, up to an overall scaling, nearly identical behaviour as ΔA_0 , including the oscillatory pattern, drift and 5th-order convergence toward the equilibrium value. The Noether charge is conserved with identical convergence to within $\Delta\mathcal{N}/\mathcal{N} \lesssim 10^{-3}$ and 10^{-4} for S06A044 and S08A06, respectively, predicting $\Delta\mathcal{N}/\mathcal{N} \lesssim 10^{-6}$ in the continuum limit for S08A06. The constraints exhibit a rapid drop to L_2 norms $\sim 10^{-9}$ due to the CCZ4 damping [44], but converge only between 1st and 4th order; cf. Fig. S3 in the Supplemental Material.

Perturbative predictions—The oscillatory behaviour of ΔA_0 in Fig. 2 can be understood in terms of linearized calculations. For this purpose, we compute the frequency χ_0 of the fundamental radial oscillation mode for our BS families using the approach of Refs. [45, 46]; cf. Sec. III in the Supplemental Material. The transitions between stable and unstable branches in Fig. 1 are characterized by zero crossings of χ_0^2 such that a real (imaginary) χ_0 implies radial (in)stability. For our BS models S06A044 and S08A06, we obtain $\chi_0^2 > 0$ as expected from their location on the rising slope of the $M(A_0)$ curve. The behaviour of these BSs, as shown in Fig. 2, exhibits excellent agreement with the perturbative predictions: numerical imperfections trigger perturbations around the equilibrium solution

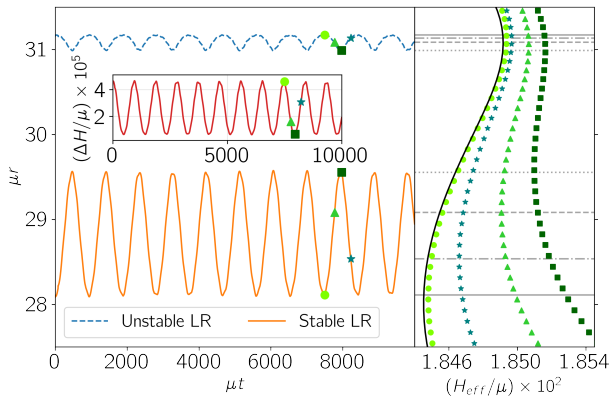


FIG. 4. (left) Areal radius of the (un)stable light ring over time as extracted from the AEP H_{eff} (right) during the time evolution of S06A044 performed with E3D. The inset shows the difference between the extrema of the AEP over time. The green markers correspond to the snapshots of the AEP given in the right panel. The gray lines indicate the positions of the extrema. The solid line is the effective potential (3) at the start of the simulation.

whose time evolution is dominated by radial oscillations with the expected frequency. We quantify this agreement by plotting in Fig. 3 for S08A06 the Fourier spectrum of $\Delta A_0(t)$, i.e. the data of Fig. 2. The spectrum peaks at the χ_0 value predicted by the perturbative calculation. The corresponding analysis for S06A044 yields similar agreement; cf. Fig. S4 in the Supplemental Material.

Light-ring structure—Having demonstrated the long-term stable behaviour of our BH mimickers S06A044 and S08A06, we now turn to the question whether their LR structure remains preserved. In a stationary and axisymmetric spacetime, a LR is defined as a null geodesic with a tangent vector field that is always a linear combination of the Killing vectors ∂_t and ∂_ϕ , assuming coordinates (t, r, θ, ϕ) adapted to the symmetry. The conditions for a LR can then be recast as follows [cf. Eqs. (1)-(8) in Ref. [18]]:

$$\partial_\mu H_\pm = 0, \quad \text{where } H_\pm := \frac{-g_{t\phi} \pm \sqrt{g_{t\phi}^2 - g_{tt}g_{\phi\phi}}}{g_{\phi\phi}}. \quad (3)$$

Furthermore, (un)stable LRs are located at local (maxima) minima of H_\pm . In spherical symmetry with adapted coordinates, H_\pm simplifies to a single potential function $H = \sqrt{-g_{tt}/g_{\phi\phi}}$.

Under the assumption that an evolved spacetime remains nearly spherically symmetric and stationary, the potential function can be approximated by an *adiabatic effective potential* (AEP) H_{eff} computed via an averaging procedure analogous to Ref. [25]. Specifically, we transform between standard Cartesian and spherical coordinates $x^\alpha = (t, x, y, z)$, $\hat{x}^\mu = (t, R, \theta, \phi)$. For a sphere of fixed coordinate radius R , we compute the proper area \mathcal{A} , the areal radius $r := \sqrt{\mathcal{A}/(4\pi)}$, and the AEP

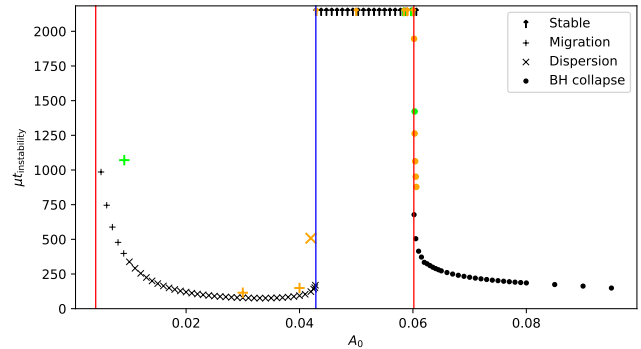


FIG. 5. Instability timescales as a function of A_0 for solitonic BSs with $\sigma_0 = 0.08$. The vertical lines mark the transition between stable and unstable branches as predicted by linear theory; cf. Fig. 1. The marker style indicates dynamical fate while the color indicates the code used: black for Sph, lime green for Axi, orange for L3D. BS models whose time evolution show no sign of instability are represented with arrows at the top of the figure.

$H_{\text{eff}}(r) = \sqrt{(\langle \alpha^2 \rangle - \langle \gamma_{ij} \beta^i \beta^j \rangle)}/r$, where α , β^i and γ_{ij} are the lapse, shift and spatial metric in Cartesian coordinates, and $\langle \cdot \rangle$ denotes averaging over the sphere. Repeating this procedure for a sequence of ~ 50 coordinate spheres with $\Delta R \approx 0.1$ across the relevant shell region, we obtain at each time t an estimate for the potential $H_{\text{eff}}(r)$. We validate the robustness of this method and the assumptions in Sec. IV of the Supplemental Material.

Our analysis of the resulting potentials for S06A044 and S08A06 indeed yields one minimum and one maximum at all t . The locations of the respective LRs exhibit minor periodic variation in line with the BS oscillations observed in the other diagnostics, but the pair of LRs remains in place with no indication of instability. We show these variations together with selected profiles of the AEP over a representative oscillation cycle in Fig. 4 for S06A044. The same behaviour, merely with smaller oscillation amplitude, is found for S08A06.

Nonlinear stability—We complement our detailed analysis of the BS models S06A044 and S08A06 with a larger set of time evolutions of the $\sigma = 0.08$ BS sequence. We have used all codes for this analysis, but restricted 3D evolutions to $\mu t \lesssim 3000$ for reasons of computational cost. In this analysis, we define the instability time as the moment when $A_0(t)$ departs by 10% from its equilibrium value. If $A_0(t)$ yields no signature of departing from the oscillatory pattern seen in Fig. 2 within $3000 \mu^{-1}$, the model is designated stable. The result is shown in Fig. 5 and fully agrees with the perturbative predictions: models on unstable branches succumb to exponentially growing perturbations on a timescale that diverges at the threshold to stable branches. These transition points coincide with extrema in the $M(A_0)$ curves, i.e. points where the oscillation frequency χ_0 of the fundamental mode switches between real and imaginary.

Concluding remarks—We have performed a series of fully nonlinear evolutions of the Einstein-Klein-Gordon equations governing the dynamics of solitonic boson stars in the thin-shell regime in 3+1 dimensions imposing spherical, axi-, octant or no symmetry. A subset of the models under consideration are ultracompact, exhibiting a pair of light rings, one of which is stable. We have evolved these objects for $\gtrsim 1000$ light crossing times, finding no evidence of an instability due to the appearance of the stable light ring, as previously conjectured [20, 24] and reported for spinning BSs [25]. We observe excellent agreement between the axisymmetric/3D evolutions and those in spherical symmetry, suggesting that the inclusion of nonspherical degrees of freedom does not significantly affect the stability of these models. Taking into account also the agreement of our numerical results with perturbative predictions for stability and fundamental radial oscillation frequencies, we interpret our findings as strong numerical evidence in favor of the stability of this class of BH mimickers.

As a cautionary note, we add that poor choices of numerical ingredients, in particular the constraint-damping parameter κ_1 of the CCZ4 formulation, can result in seemingly plausible instabilities of our thin-shell BSs. With $M\kappa_1 \gg 0.1$, for example, both models S06A044 and S08A06 collapse to a BH; the erroneous nature of these simulations reveals itself only through large and growing constraint violations and complete lack of convergence.

If the presence of the stable light ring is not sufficient to destroy these solitonic boson stars, this family of spherically symmetric models, i.e. with quantized spin zero, as well as similar UCOs, can be considered as viable black-hole mimickers again. The thin-shell solutions under consideration here can mimic the phenomenology of black holes in several different ways, as for example in the GW emission from binaries [17] or the creation of BH like shadows in VLBI images [47]. Figure 6 illustrates how the S06A044 model could resemble a Schwarzschild BH with the same ADM mass in the presence of an equatorial, optically thin accretion disk. The image of the BS clearly displays additional structure toward the center of the image, which is a result of the absence of a horizon

as well as the pair of light rings. The outermost direct emission band, as well as the first lensed photon ring are nearly indistinguishable for both images.

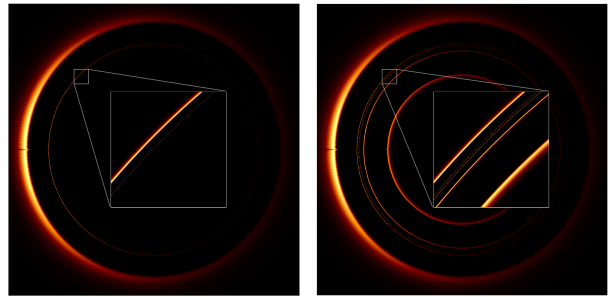


FIG. 6. Side-by-side comparison of ray-traced images of (left) a Schwarzschild BH and (right) the S06A044 model of the same ADM mass. The color scale indicates the observed brightness intensity, in arbitrary units, from a simple geometrically thin disk located in the equatorial plane. Both panels also provide a close-up of the photon ring region, exhibiting their fractal structure. Images are obtained with FOORT [48, 49].

Acknowledgments—G.A.M. is supported by the Cambridge Trust at the University of Cambridge. S.S. is supported by the Centre for Doctoral Training at the University of Cambridge funded through STFC. T.E. acknowledges the Perimeter Institute for Theoretical Physics, supported by the Government of Canada through the Department of Innovation, Science and Economic Development and by the Province of Ontario through the Ministry of Colleges and Universities. This work has been supported by STFC Research Grant No. ST/V005669/1. We acknowledge support by the NSF Grants No. PHY-090003, No. PHY-1626190, and No. PHY-2110594; DiRAC projects No. ACTP284 and No. ACTP238; STFC capital Grants No. ST/P002307/1, No. ST/R002452/1, No. ST/I006285/1, and No. ST/V005618/1; and STFC operations Grant No. ST/R00689X/1. Computations were done on the CSD3 and Fawcett (Cambridge), Cosma (Durham), Niagara (Toronto), Narval (Montreal), Stampede2 (TACC) and Expanse (SDSC) clusters.

-
- [1] S. Bowyer, E. T. Byram, T. A. Chubb, and H. Friedmann, *Science* **147**, 394 (1965).
 - [2] C. Hazard, M. B. Mackey, and A. J. Shimmins, *Nature* **197**, 1037 (1963).
 - [3] M. Schmidt, *Nature* **197**, 1040 (1963).
 - [4] B. P. Abbott *et al.*, *Phys. Rev. Lett.* **116**, 061102 (2016), arXiv:1602.03837 [gr-qc].
 - [5] R. Abbott *et al.* (KAGRA, VIRGO, LIGO Scientific), *Phys. Rev. X* **13**, 041039 (2023), arXiv:2111.03606 [gr-qc].
 - [6] R. Abbott *et al.* (LIGO Scientific, VIRGO, KAGRA), (2021), arXiv:2112.06861 [gr-qc].
 - [7] K. Akiyama *et al.* (Event Horizon Telescope), *Astrophys. J. Lett.* **875**, L1 (2019), arXiv:1906.11238 [astro-ph.GA].
 - [8] K. Akiyama *et al.* (Event Horizon Telescope), *Astrophys. J. Lett.* **930**, L12 (2022), arXiv:2311.08680 [astro-ph.HE].
 - [9] J. L. Synge, *Mon. Not. Roy. Astron. Soc.* **131**, 463 (1966).
 - [10] V. Cardoso, A. S. Miranda, E. Berti, H. Witek, and V. T. Zanchin, *Phys. Rev. D* **79**, 064016 (2009), arXiv:0812.1806 [hep-th].
 - [11] K. Jusufi, *Phys. Rev. D* **101**, 084055 (2020), arXiv:1912.13320 [gr-qc].
 - [12] Y. Koga, N. Asaka, M. Kimura, and K. Okabayashi, *Phys. Rev. D* **105**, 104040 (2022), arXiv:2202.00201 [gr-qc].
 - [13] S. H. Völkel, N. Franchini, E. Barausse, and E. Berti, *Phys. Rev. D* **106**, 124036 (2022), arXiv:2209.10564 [gr-qc].

- qc].
- [14] D. Pedrotti and M. Calzà, Phys. Rev. D **111**, 124056 (2025), arXiv:2504.01909 [gr-qc].
- [15] S. W. Hawking and G. F. R. Ellis, *The Large Scale Structure of Space-Time* (Cambridge University Press, 1973).
- [16] S. D. Mathur, Classical and Quantum Gravity **26**, 224001 (2009).
- [17] T. Evstafyeva, U. Sperhake, I. Romero-Shaw, and M. Agathos, Phys. Rev. Lett. **133**, 131401 (2024), arXiv:2406.02715 [gr-qc], arXiv:2406.02715 [gr-qc].
- [18] P. V. P. Cunha, E. Berti, and C. A. R. Herdeiro, Phys. Rev. Lett. **119**, 251102 (2017), arXiv:1708.04211 [gr-qc].
- [19] P. V. P. Cunha and C. A. R. Herdeiro, Phys. Rev. Lett. **124**, 181101 (2020), arXiv:2003.06445 [gr-qc].
- [20] J. Keir, Class. Quant. Grav. **33**, 135009 (2016), arXiv:1404.7036 [gr-qc].
- [21] P. Bizoń and A. Rostworowski, Phys. Rev. Lett. **107**, 031102 (2011), arXiv:1104.3702 [gr-qc].
- [22] G. Holzegel and J. Smulevici, Commun. Pure Appl. Math. **66**, 1751 (2013), arXiv:1110.6794 [gr-qc].
- [23] G. Holzegel and J. Smulevici, Anal. Part. Diff. Eq. **7**, 1057 (2014), arXiv:1303.5944 [gr-qc].
- [24] V. Cardoso, L. C. B. Crispino, C. F. B. Macedo, H. Okawa, and P. Pani, Phys. Rev. D **90**, 044069 (2014), arXiv:1406.5510 [gr-qc].
- [25] P. V. P. Cunha, C. Herdeiro, E. Radu, and N. Sanchis-Gual, Phys. Rev. Lett. **130**, 061401 (2023), arXiv:2207.13713 [gr-qc].
- [26] P. V. P. Cunha, (2025), arXiv:2503.00117 [gr-qc].
- [27] N. Siemonsen, Phys. Rev. Lett. **133**, 031401 (2024), arXiv:2404.14536 [gr-qc].
- [28] G. Guo, P. Wang, and Y. Zhang, (2024), arXiv:2403.02089 [gr-qc].
- [29] G. Benomio, A. Cárdenas-Avendaño, F. Pretorius, and A. Sullivan, (2024), arXiv:2411.17445 [gr-qc].
- [30] J. Redondo-Yuste and A. Cárdenas-Avendaño, (2025), arXiv:2502.18643 [gr-qc].
- [31] L. G. Collodel and D. D. Doneva, Phys. Rev. D **106**, 084057 (2022), arXiv:2203.08203 [gr-qc].
- [32] T. Evstafyeva, R. Rosca-Mead, U. Sperhake, and B. Bruegmann, Phys. Rev. D **108**, 104064 (2023), arXiv:2310.05200 [gr-qc].
- [33] T. W. Baumgarte and S. L. Shapiro, Phys. Rev. D **59**, 024007 (1998), gr-qc/9810065.
- [34] M. Shibata and T. Nakamura, Phys. Rev. D **52**, 5428 (1995).
- [35] D. Alic, C. Bona-Casas, C. Bona, L. Rezzolla, and C. Palenzuela, Phys. Rev. D **85**, 064040 (2012), arXiv:1106.2254 [gr-qc].
- [36] W. G. Cook, P. Figueras, M. Kunesch, U. Sperhake, and S. Tunyasuvunakool, Int. J. Mod. Phys. D **25**, 1641013 (2016), arXiv:1603.00362 [gr-qc].
- [37] “ExoZvezda code; <https://github.com/GRTLCollaboration/ExoZvezda>,” GitHub repository (2024).
- [38] M. Radia, U. Sperhake, A. Drew, K. Clough, P. Figueras, E. A. Lim, J. L. Ripley, J. C. Aurrekoetxea, T. França, and T. Helfer, Class. Quant. Grav. **39**, 135006 (2022), arXiv:2112.10567 [gr-qc].
- [39] T. Andrade *et al.*, J. Open Source Softw. **6**, 3703 (2021), arXiv:2201.03458 [gr-qc].
- [40] M. Adams *et al.*, *Chombo Software Package for AMR Applications - Design Document*, Tech. Rep. LBNL-6616E (Lawrence Berkeley National Laboratory, 2019).
- [41] U. Sperhake, Phys. Rev. D **76**, 104015 (2007), gr-qc/0606079.
- [42] Allen, G. and Goodale, T. and Massó, J. and Seidel, E., in *Proceedings of Eighth IEEE International Symposium on High Performance Distributed Computing, HPDC-8, Redondo Beach, 1999* (IEEE Press, Piscataway, New Jersey, United States, 1999).
- [43] E. Schnetter, S. H. Hawley, and I. Hawke, Class. Quant. Grav. **21**, 1465 (2004), gr-qc/0310042.
- [44] D. Alic, W. Kastaun, and L. Rezzolla, Phys. Rev. D **88**, 064049 (2013), arXiv:1307.7391 [gr-qc].
- [45] M. Gleiser and R. Watkins, Nucl. Phys. B **319**, 733 (1989).
- [46] B. Kain, Phys. Rev. D **103**, 123003 (2021), arXiv:2106.01740 [gr-qc].
- [47] J. L. Rosa, C. F. B. Macedo, and D. Rubiera-Garcia, Phys. Rev. D **108**, 044021 (2023), arXiv:2303.17296 [gr-qc].
- [48] D. R. Mayerson, “FOORT: Flexible Object-Oriented Ray Tracing; <https://github.com/drmayerson/FOORT>,”.
- [49] D. R. Mayerson, F. Bacchini, and S. J. Staelens, (in prep.).

Supplemental Material

I. CONVERGENCE ANALYSIS

Light rings: We check convergence of the computed light ring (LR) radii for the S08A06 model by comparing results obtained at resolutions $\mu h \in \{1/12, 1/16, 1/20\}$ and display in Fig. S1 the resulting areal radii of the stable LR as functions of time. At low resolution the LR radius exhibits a linear drift, much like what was observed for the central amplitude and Kretschmann scalar (cf. Fig. 2 in the main text). Again, this drift converges away at 5th order, and the Richardson extrapolated values, obtained from the two highest-resolution runs and displayed in Fig. S2, oscillate around constant values.

For the S06A044 model, we observe no discernible drift and increasing the resolution merely results in convergence of the regular oscillations. Again, this underlines that the oscillatory perturbation of the S06A044 model is dominated by the quality of the initial data rather than details of the evolution.

In Fig. S2 we see that the oscillation amplitude of the stable LR is slightly larger than that of the unstable LR. This effect is more pronounced for the S06A044 model displayed in Fig. 4 of the main text. The reason in both cases is that the unstable light ring is - to good approximation - outside the thin shell, fixing its location close to the Schwarzschild value by Birkhoff's theorem. The stable light ring, on the other hand, is located in the interior of the star, and therefore affected more strongly by the perturbation.

2D code: We next discuss the convergence results for the S08A06 model obtained in axisymmetry with the Axi code. Using $\mu h = 1/8$, $\mu h = 1/12$ and $\mu h = 1/16$ on the innermost refinement level for the low, medium and high resolutions, respectively, we obtain convergence between fourth and fifth order for the scalar field amplitude; cf. top panel of Fig. S3. In the bottom panels of the

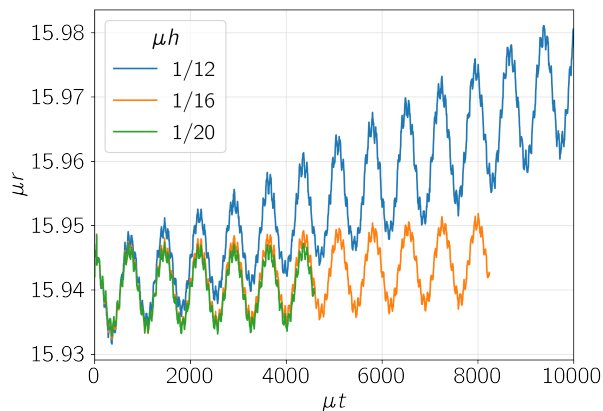


FIG. S1. Evolution of the areal radius of the stable LR for the S08A06 model obtained with the E3D code using different resolutions indicated in the legend. The differences between the curves yield convergence at 5th order.

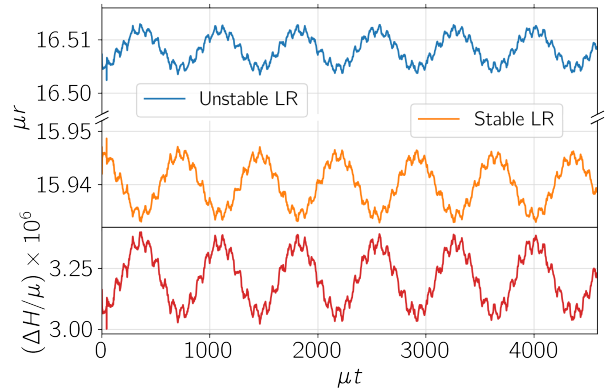


FIG. S2. Richardson extrapolation (5th order) of the LR areal radii of the S08A06 model based on the runs at resolutions $\mu h = 1/16, 1/20$. The bottom panel shows the Richardson extrapolated evolution of the potential difference between the extrema of the AEP.

figure, we also monitor the volume-weighted L_2 norms of the constraint violations. We find first-order convergence in the Hamiltonian constraint at very early times which gradually transitions to fourth order at $\mu t \approx 20000$ where it persists throughout the remainder of the simulation. The momentum constraint $\mathcal{M} := (\mathcal{M}_x^2 + \mathcal{M}_y^2)^{1/2}$ on the other hand rapidly reaches convergence between fourth and fifth order.

II. ADDITIONAL RESULTS FOR $\sigma_0 = 0.06$

In this section we present results for the $\sigma_0 = 0.06$ family of models, supplementing those presented for $\sigma_0 = 0.08$ in the main text. In Fig. S4, we compare the power spectrum of central scalar-amplitude oscillations to the radial oscillation frequency, computed with perturbation theory. In this case the larger error in our initial data causes the system to migrate early on to a boson-star (BS) model with slightly smaller central scalar amplitude than the initial value $A_0 = 0.044$. Following Ref. [S1] we take this effect into account by computing the radial frequency for a BS model with an amplitude averaged over several oscillation cycles, $\langle A_0 \rangle = 0.04394$. Once again, we find very good agreement between results from the perturbative analysis and the codes enforcing different symmetry assumptions.

In Fig. S5, we show timescales of instability for a sample of BS models with $\sigma_0 = 0.06$. As before, we use the time at which the absolute change in the central amplitude $|\Delta A_0(t)|$ exceeds 10% of the initial central amplitude $\Delta A_0(0)$. Once again, we find that the predictions of the linear radial perturbation theory are borne out by all codes regardless of symmetry assumptions. Models on the first unstable branch either migrate or disperse depending on the sign of the binding energy, and models on

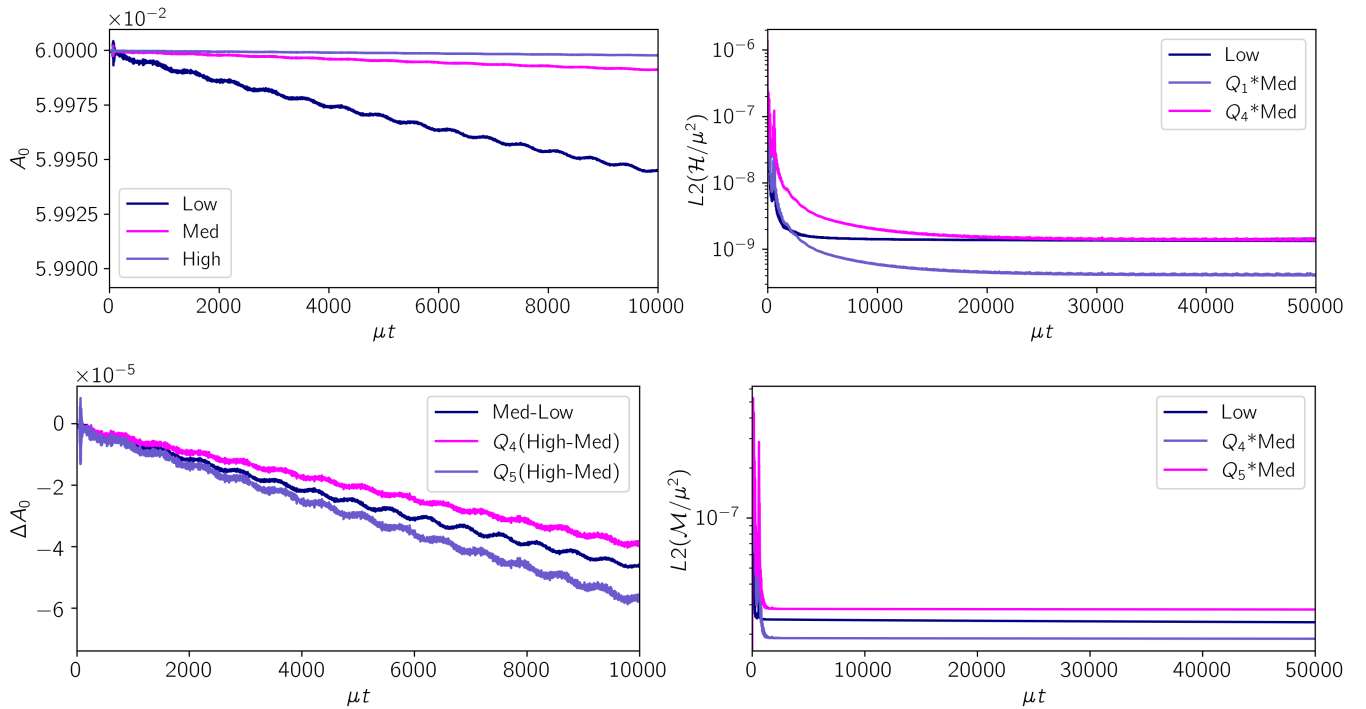


FIG. S3. The left (right) panels illustrate convergence results obtained from `Axi` simulations of the `S08A06` model for the scalar field amplitude (volume-weighted L_2 norms of the Hamiltonian and momentum constraints). We amplify the differences and constraint magnitudes by factors Q_n as expected for n^{th} -order convergence.

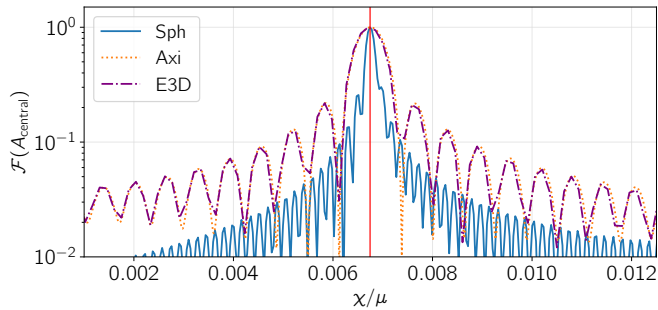


FIG. S4. Power spectrum of $\Delta A_0(t)$ for the BS model `S06A044`; the red line marks the fundamental radial mode frequency χ_0 . Units on the vertical axis are arbitrary.

the second unstable branch always collapse to a BH. We emphasize that the specific time values depend on factors such as resolution, gauge, evolution method and numerical parameter choices or mesh refinement; values determined with different codes therefore exhibit some variation but always agree on stability or instability. Note also that for some values of A_0 , multiple BS models exist. In those cases, the two lower-mass models are always stable while the heaviest BS may be stable or not, in accordance with the predictions of linear theory.

III. RADIAL OSCILLATION FREQUENCIES

In this section we discuss in detail the method used to compute fundamental radial oscillation frequencies for solitonic BSs. Here, we use overdots to denote time derivatives and primes for radial derivatives.

We begin with a spherically symmetric metric ansatz,

$$ds^2 = -\alpha^2(t, r)dt^2 + X^2(t, r)dr^2 + r^2 d\Omega_2^2. \quad (\text{S1})$$

Decomposing the complex scalar field into two real fields, $\varphi(t, r) = \varphi_1 + i\varphi_2$, the Einstein-Klein-Gordon equations become,

$$\frac{X'}{X} = \frac{1 - X^2}{2r} + 2\pi r X^2 \left(\frac{|\dot{\varphi}|^2}{\alpha^2} + \frac{|\varphi'|^2}{X^2} + V \right), \quad (\text{S2})$$

$$\frac{\alpha'}{\alpha} = -\frac{1 - X^2}{2r} + 2\pi r X^2 \left(\frac{|\dot{\varphi}|^2}{\alpha^2} + \frac{|\varphi'|^2}{X^2} - V \right), \quad (\text{S3})$$

$$\varphi_i'' = \left(\frac{X'}{X} - \frac{\alpha'}{\alpha} - \frac{2}{r} \right) \varphi_i' + \frac{X^2 \dot{\alpha} + X \alpha \dot{X}}{\alpha^3} \dot{\varphi}_i + \frac{X^2}{\alpha^2} \ddot{\varphi}_i, \quad (\text{S4})$$

$$\alpha'' = \frac{X \ddot{X}}{\alpha} - \frac{X \dot{X} \dot{\alpha}}{\alpha^2} + \frac{X' \alpha'}{X} - \frac{\alpha'}{r} + \frac{\alpha X'}{r X} + 4\pi \alpha \left(\frac{X^2}{\alpha^2} |\dot{\varphi}|^2 - |\varphi'|^2 - 4X^2 V \right). \quad (\text{S5})$$

We solve Eqs. (S2)-(S4) using the ansatz $\varphi(t, r) = A(r)e^{i\omega t}$ to obtain a background solution henceforth

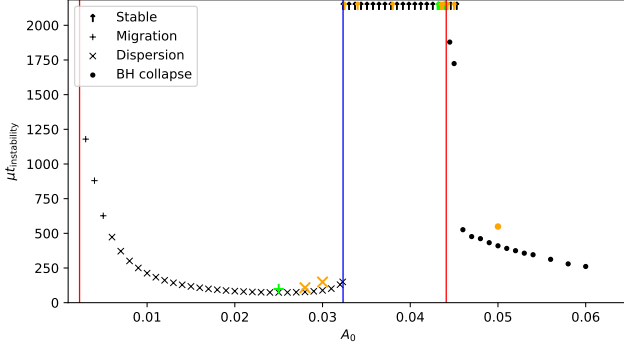


FIG. S5. Instability timescales as a function of A_0 for solitonic BSs with $\sigma_0 = 0.06$. The vertical lines mark the transition between stable and unstable branches as predicted by linear theory. The marker style indicates the dynamical fate while colour indicates the code used: black for **Sph**, lime green for **Axi**, orange for **E3D**. BS models whose time evolution shows no sign of instability are represented with arrows at the top of the figure.

denoted by $\{A_b(r), \alpha_b(r), X_b(r), \omega\}$. The background scalar-field amplitude in particular satisfies

$$A_b'' = -\frac{\omega^2 X_b^2}{\alpha_b^2} A_b + A_b' \left(\frac{X_b'}{X_b} - \frac{\alpha_b'}{\alpha_b} - \frac{2}{r} \right) + X_b^2 A_b V'(A_b^2), \quad (S6)$$

We perturb the BS background by introducing the perturbations $\delta\psi_1$, $\delta\psi_2$, $\delta\nu$ and $\delta\lambda$ according to

$$\begin{aligned} \varphi &= e^{i\omega t} (\psi_1 + i\psi_2), \\ \psi_1 &= A_b(1 + \delta\psi_1), & \psi_2 &= A_b\delta\psi_2, \\ \alpha &= \alpha_b \left(1 + \frac{1}{2}\delta\nu \right), & X &= X_b \left(1 + \frac{1}{2}\delta\lambda \right). \end{aligned} \quad (S7)$$

Substituting this expansion into Eqs. (S2), (S4), (S5), taking the difference between Eqs. (S3) and (S2), and linearizing, we obtain

$$\begin{aligned} \delta\psi_1'' &= X_b^2 \left(1 - \frac{\omega^2}{\alpha_b^2} - \frac{8A_b^2}{\sigma_0^2} + \frac{12A_b^4}{\sigma_0^4} \right) \delta\lambda + \frac{X_b^2}{\alpha_b^2} \delta\ddot{\psi}_1 + \frac{16A_b^2 X_b^2}{\sigma_0^2} \left(\frac{3A_b^2}{\sigma_0^2} - 1 \right) \delta\psi_1 + \frac{A_b'}{2A_b} (\delta\lambda' + 4\delta\psi_1' - \delta\nu') \\ &\quad + \frac{\omega X_b^2}{\alpha_b^2} (2\delta\dot{\psi}_2 - \omega\delta\nu) + \left(\frac{X_b'}{X_b} - \frac{\alpha_b'}{\alpha_b} - \frac{2}{r} \right) \delta\psi_1', \end{aligned} \quad (S8)$$

$$\begin{aligned} \delta\lambda' &= \left(\frac{2X_b'}{X_b} - \frac{1}{r} - 4\pi r (A_b')^2 \right) \delta\lambda + 8\pi r X_b^2 \left(A_b^2 + \frac{(A_b')^2}{X_b^2} + \frac{\omega^2 A_b^2}{\alpha_b^2} + \frac{12A_b^6}{\sigma_0^4} - \frac{6A_b^4}{\sigma_0^2} \right) \delta\psi_1 \\ &\quad + \frac{4\pi r \omega A_b^2 X_b^2}{\alpha_b^2} (\omega\delta\nu + 2\delta\dot{\psi}_2) + 8\pi r A_b' A_b \delta\psi_1'. \end{aligned} \quad (S9)$$

$$\begin{aligned} \delta\ddot{\lambda} &= \frac{2\alpha_b}{X_b^2} \left[\frac{\alpha_b X_b'}{r X_b} + \alpha_b' \left(\frac{X_b'}{X_b} - \frac{1}{r} \right) - \alpha_b'' - 4\pi\alpha_b (A_b')^2 \right] \delta\lambda - \frac{16\pi\alpha_b^2}{\omega X_b} \left[\frac{(A_b')^2}{X_b^2} + A_b^2 - \frac{8A_b^4}{\sigma_0^2} + \frac{12A_b^6}{\sigma_0^4} - \omega^2 A_b^2 \right] \delta\psi_1 \\ &\quad + 8\pi\omega A_b^2 (\omega\delta\nu - 2\delta\dot{\psi}_2) + \frac{1}{r X_b} \left(\frac{r\alpha_b^2 \delta\nu'}{X_b} \right)' + \frac{16\pi\alpha_b^2 A_b' A_b}{X_b^2} \delta\psi_1' - \frac{1}{r X_b^2} (\alpha_b^2 + r\alpha_b \alpha_b') \delta\lambda'. \end{aligned} \quad (S10)$$

$$\delta\lambda' - \delta\nu' = 2 \left(\frac{X_b'}{X_b} - \frac{\alpha_b'}{\alpha_b} - \frac{1}{r} \right) + 16\pi r A_b^2 X_b^2 \left(1 - \frac{8A_b^2}{\sigma_0^2} + \frac{12A_b^4}{\sigma_0^4} \right). \quad (S11)$$

Next, we make the harmonic ansatz $\delta\psi_1(t, r) = e^{i\chi t} f(r)$, $\delta\lambda(t, r) = e^{i\chi t} g(r)$ with $\chi \in \mathbb{C}$ to be determined. The resulting system of two pulsation equations is self-adjoint, so that, in analogy to the BS frequencies ω , the radial oscillation frequencies χ form an infinite discrete sequence $\chi_0^2 < \chi_1^2 < \dots$, where the solution with eigenvalue χ_n^2 is regular with n zero crossings in f and g . A negative χ_0^2 corresponds to a radial instability, while $\chi_0^2 > 0$ guarantees (linear) radial stability.

To obtain the first pulsation equation, we solve Eq. (S9) for $\delta\dot{\psi}_2$ and substitute into Eq. (S8) to obtain an equation that depends on $\delta\nu$ only through its radial derivative which, in turn, can be removed using Eq. (S11). For the second pulsation equation, we combine Eqs. (S6), (S9) and (S10) to obtain an equation that depends on $\delta\nu'$ and $\delta\nu''$ but not $\delta\nu$ directly. By using Eq. (S11), its derivative and Eq. (S6), we can eliminate $\delta\nu$ completely and thus arrive at our final system of two ODEs,

$$\begin{aligned}
f'' = X_b^2 & \left[2 + \frac{2(A'_b)^2}{X_b^2 A_b^2} + \frac{2\omega^2 - \chi^2}{\alpha_b^2} + 8\pi r A_b A'_b - \frac{32A_b^2}{\sigma_0^2} (1 + 2\pi r A_b^2 A'_b) + \frac{8A_b^4}{\sigma_0^4} (9 + 12\pi r A_b A'_b) \right] f \\
& + \left[X_b^2 \left(1 - \frac{8A_b^2}{\sigma_0^2} + \frac{12A_b^4}{\sigma_0^4} \right) - \frac{1}{4\pi r^2 A_b^2} - \frac{(A'_b)^2}{A_b^2} - \frac{A'_b}{r A_b} - \frac{A'_b \alpha'_b}{A_b \alpha_b} + \frac{X'_b}{X_b A_b} \left(A'_b + \frac{1}{2\pi r A_b} \right) \right] g \\
& + \left(\frac{X'_b}{X_b} - \frac{\alpha'_b}{\alpha_b} - \frac{2}{r} \right) f' - \frac{1}{4\pi r A_b^2} g',
\end{aligned} \tag{S12}$$

$$\begin{aligned}
g'' = 32\pi r X_b^2 & \left[A_b A'_b + \frac{\alpha'_b A_b^2}{\alpha_b} - \frac{8A_b^3}{\sigma_0^2} \left(2A'_b + \frac{A_b \alpha'_b}{\alpha_b} \right) + \frac{X'_b}{X_b} \left(A_b^2 - \frac{4A_b^4}{\sigma_0^2} + \frac{6A_b^6}{\sigma_0^4} - \frac{(A'_b)^2}{X_b^2} \right) \right] \\
& + \frac{12A_b^5}{\sigma_0^4} \left(3A'_b + \frac{A_b \alpha'_b}{\alpha_b} \right) \Big] f + 3 \left(\frac{X'_b}{X_b} - \frac{\alpha'_b}{\alpha_b} \right) g' + \left[16\pi (A'_b)^2 - \frac{\chi^2 X_b^2 - 2(\alpha'_b)^2}{\alpha_b^2} - \frac{4\alpha'_0}{r \alpha_b} + \frac{2}{r^2} \right. \\
& \left. + \frac{2}{X_b} \left(X_b'' + \frac{2\alpha'_b X'_b}{\alpha_b} - \frac{2(X'_b)^2}{X_b} - \frac{X'_b}{r} \right) \right] g + 16\pi r X_b^2 A_b^2 \left(1 - \frac{8A_b^2}{\sigma_0^2} + \frac{12A_b^4}{\sigma_0^4} - 2\frac{A_b A'_b}{r X_b^2} \right) f'.
\end{aligned} \tag{S13}$$

Before we can solve this system numerically, we must determine its behavior in the limit $r \rightarrow 0$. Bearing in mind the even parity of scalar functions across $r = 0$ and using our freedom to rescale the perturbations, we can expand them without loss of generality as $f = 1 + \frac{\gamma}{2} r^2 + \mathcal{O}(r^4)$ and $g = \beta + \frac{\gamma}{2} r^2 + \mathcal{O}(r^4)$. Inserting into Eqs. (S12) and (S13) gives us

$$\begin{aligned}
a = \frac{1}{3} & \left(2 + \frac{2\omega^2 - \chi^2}{\alpha_b(0)^2} - \frac{32A_b(0)^2}{\sigma_0^2} + \frac{72A_b(0)^4}{\sigma_0^4} \right) \\
& - \frac{\gamma}{8\pi A_b(0)^2},
\end{aligned} \tag{S14}$$

as well as $\beta = 0$ at leading order. There is a degeneracy, however, at the following order so that γ remains undetermined. In consequence, we have *two* undetermined parameters, χ and γ , which need to be finetuned to obtain regular spacetimes.

To do this, we need two appropriate boundary conditions at $r \rightarrow \infty$. Asymptotic flatness requires that $\delta\lambda$ vanishes at infinity. The second condition is obtained by enforcing that the perturbation conserves the Noether charge

$$\mathcal{N} = \int \sqrt{-\det g} J^0 d^3x, \quad J^\mu = \frac{i}{2} g^{\mu\nu} (\bar{\varphi} \partial_\nu \varphi - \varphi \partial_\nu \bar{\varphi}),$$

compliant with the scalar field's $U(1)$ symmetry. The variation in the Noether charge is given by

$$\delta\mathcal{N} = 4\pi \int_0^\infty \frac{A_b^2 r^2}{\alpha_b} dr \left[\omega X_b (\delta\lambda - \delta\nu) + 2\delta\psi_2 + 4\omega\delta\psi_1 \right].$$

Combining with Eq. (S9) allows us to eliminate $\delta\nu$ whence, using the background equations (S2)-(S6), we can write the integrand as a total derivative and find

$$\delta\mathcal{N} = \frac{1}{\omega X_b} (8\pi r^2 \alpha_b A_b A'_b f - r \alpha_b g) \Big|_{r=0}^\infty. \tag{S15}$$

Despite appearances, the first term is nonnegligible in this expression due to the exponential behavior of f which vanishes only for precise choices of the shooting parameters χ and γ . Thus, for regular perturbations which remain finite at $r = 0$, the condition $\delta N = 0$ supplies a second boundary condition at infinity. Finally, it is worth noting that because $\delta\lambda$ is related to the perturbation of the total mass,

$$\delta\lambda = \frac{2X_b^2}{r} \delta M, \tag{S16}$$

at large radius, our two conditions amount to enforcing that both the mass and particle number of the BS are unchanged by the perturbation. In practice, we solve Eqs. (S12) and (S13) using a standard fourth-order Runge-Kutta method, shooting for the undetermined values χ and γ for each model. We determine these two parameters using a bisection method similar to that commonly used to determine the frequency ω for equilibrium BS models. Interestingly, we encounter the same challenging accuracy requirements in our determination of χ and γ for thin-shell BSs as observed when calculating the BS frequency ω ; therefore we also compute the radial oscillation spectrum using quadruple precision.

With this method, we can compute real and imaginary χ_0 as well as overtone frequencies. In this work, we wish to identify stable systems and therefore restrict our attention to identifying regimes of positive versus negative χ_0^2 . The point in the BS parameter space at which models transition from stable to unstable is marked by the existence of a zero-frequency perturbation, $\chi_0^2 = 0$. Such zero-frequency perturbations can only exist where two neighboring solutions with the same mass (or, equivalently, Noether charge) exist. The condition $dM/dA_0 = 0$ is therefore a necessary but insufficient criterion for the transition of a radial oscillation mode from stability to instability. For mini BSs, there exists only one stable branch consisting of models with

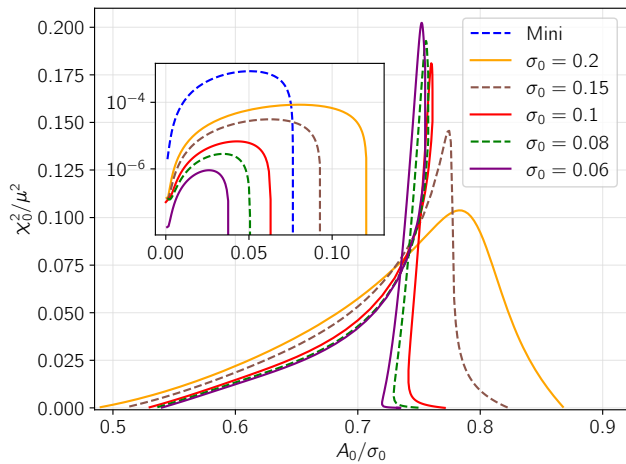


FIG. S6. Fundamental radial oscillation frequencies χ_0^2 against central amplitude A_0 for mini and solitonic BSs with a variety of σ_0 -values. The main figure shows the second stable branch, while the inset shows the first. Central amplitudes are rescaled by the appropriate σ_0 -value, apart from mini BSs, which undergo no rescaling.

central amplitude smaller than that corresponding to the maximum-mass model [S2]. However, for solitonic models with sufficiently small σ_0 , a second stable branch emerges; see e.g. Fig. 4 in Ref. [S3] for representative examples.

We illustrate the existence of two stable branches for solitonic BSs in Fig. S6. There, for each family of BSs, a positive $\chi_0^2 > 0$ is obtained across two disjoint regions in the parameter space, including the ultracompact thin-shell models in the regime where M and ω are multi-valued functions of A_0 . Indeed, the curve $\chi_0^2(A_0)$ also becomes multivalued for these σ_0 -values, and self-intersects. In the case of mini BSs, our results are compatible with those computed in Ref. [S1].

IV. ADIABATIC EFFECTIVE POTENTIAL

To assess whether our BSs remains ultracompact throughout their evolution, we need to check whether the light-ring structure persists. As the BS is evolved in 3+1 dimensions, the spacetime generally loses its spherical symmetry as a result of numerical errors and gauge effects that excite asymmetric modes. In terms of the 3+1 metric

$$ds^2 = -\alpha^2 dt^2 + \gamma_{ij} (dx^i + \beta^i dt) (dx^j + \beta^j dt), \quad (\text{S17})$$

where α, β^i and γ_{ij} are the standard lapse, shift and spatial metric, this means that the shift will become non-zero, and the spatial metric will deviate from spherical symmetry. In principle, the effective potential in the form

$$H(\tilde{r}, \tilde{\theta}) = \sqrt{\frac{-g_{\tilde{t}\tilde{t}}}{g_{\tilde{\phi}\tilde{\phi}}}} \quad (\text{S18})$$

is only defined for stationary spacetimes that exhibit spherical symmetry; here a tilde distinguishes coordinates of such a spacetime from those used in our approximately symmetric numerical evolutions.

Given that our evolutions are expected to approximately respect the symmetries of the initial data, the presence of (stable) bound geodesics can still be deduced from an Adiabatic Effective Potential (AEP). To derive the AEP, we adapt the approach of Ref. [S4] from (approximate) axisymmetry and apply it to our spherically symmetric setting. Under the assumptions outlined in that work, the metric component $g_{\tilde{t}\tilde{t}}$ in the effective potential (S18) can be replaced by the evolution variables of the 3+1 line element (S17) according to

$$g_{\tilde{t}\tilde{t}} \rightarrow -\langle \alpha^2 \rangle + \langle \gamma_{ij} \beta^i \beta^j \rangle. \quad (\text{S19})$$

Here the brackets denote averaging over a sphere of fixed coordinate radius $R = \sqrt{x^2 + y^2 + z^2}$ and x, y, z are the Cartesian coordinates of the evolution grid. We convert R into the areal radius r by calculating the proper area \mathcal{A} of the sphere¹

$$r^2 = \frac{\mathcal{A}}{4\pi} = \frac{1}{4\pi} \oint_{S^2} \sqrt{\det q} d\theta d\phi, \quad (\text{S20})$$

where q is the metric induced on the sphere. Mapping between Cartesian coordinates (x, y, z) and angular coordinates (R, θ, ϕ) , the induced metric becomes

$$\begin{aligned} q_{\theta\theta} &= z^2(\gamma_{xx} \cos^2 \phi + \gamma_{yy} \sin^2 \phi) + \gamma_{zz} R^2 \sin^2 \theta \\ &\quad + \gamma_{xy} z^2 \sin(2\phi) - 2zR \sin \theta (\gamma_{xz} \cos \phi + \gamma_{yz} \sin \phi), \\ q_{\phi\phi} &= \gamma_{xx} y^2 - 2\gamma_{xy} xy + \gamma_{yy} x^2, \\ q_{\theta\phi} &= \gamma_{yy} xz \sin \phi - \gamma_{xx} yz \cos \phi + \gamma_{xy} z(x \cos \phi - y \sin \phi) \\ &\quad + R \sin \theta (\gamma_{xz} y - \gamma_{yz} x). \end{aligned}$$

In the equatorial plane $\tilde{\theta} = \frac{\pi}{2}$ of the stationary and spherically symmetric spacetime, we have $g_{\tilde{\phi}\tilde{\phi}} = \tilde{r}^2$. Replacing $\tilde{r} \rightarrow r$ and using Eqs. (S18)-(S20) we now define the AEP as

$$H_{\text{eff}}(r) = \sqrt{\frac{\langle \alpha^2 \rangle - \langle \gamma_{ij} \beta^i \beta^j \rangle}{r}}. \quad (\text{S21})$$

In the idealized case where our simulation is perfectly spherically symmetric and stationary, Eq. (S21) reduces to Eq. (S18). As long as this AEP has extrema we have evidence that the BS is still ultracompact, featuring a pair of (perturbed) light rings. In practice, we extract the AEP at a number of coordinate radii with resolution $\Delta R \approx 0.1$ in the range where we expect the light rings to be.

¹ Note that it is not guaranteed that the coordinate sphere actually corresponds to a sphere in terms of the areal radius. Again, if the evolution remains sufficiently close to spherical symmetry, this is a good approximation.

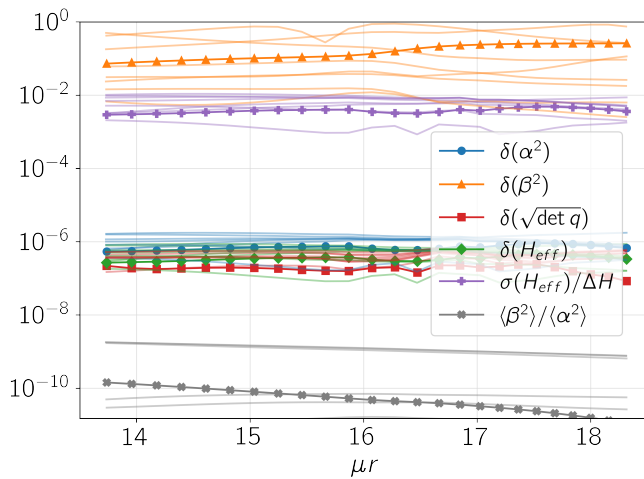


FIG. S7. Diagnostics to assess the deviations from spherical symmetry and stationarity for **S08A06**. Brackets denote averaging over an extraction sphere, whereas σ denotes the standard deviation from this average value. The relative standard deviation is $\delta(X) \equiv \sigma(X)/\langle X \rangle$, and ΔH denotes the potential difference between the two extrema of the AEP. The lines with markers correspond to time $\mu t = 75$, after early gauge dynamics have settled down. The other lines correspond to extractions at later times ($\mu t \in \{250, 500, \dots, 2000\}$) to illustrate that the conclusions also hold at later times.

In order to quantify the deviation from spherical symmetry, we compute the variation of the relevant quantities over the extraction spheres. For this purpose, we define the relative standard deviation of a variable X as

$$\delta(X) \equiv \frac{\sigma(X)}{\langle X \rangle} \equiv \frac{\sqrt{\langle (X - \langle X \rangle)^2 \rangle}}{\langle X \rangle}, \quad (\text{S22})$$

Figure S7 shows the relative standard deviation for the individual terms of Eq. (S21), as well as that of the AEP itself, as obtained for 192 points on each sphere.

The largest relative deviation from spherical symmetry is seen for $\beta^2 \equiv \gamma_{ij}\beta^i\beta^j$, where $\delta(\beta^2) \gtrsim 10^{-2}$, reaching order unity at some times; this is merely a consequence of our definition (S22) and the near-zero average $\langle \beta^2 \rangle$. This interpretation is supported by the very small ratio $\langle \beta^2 \rangle / \langle \alpha^2 \rangle \lesssim 10^{-9}$. The relative standard deviation of the remaining variables is $\lesssim 10^{-6}$, suggesting that the spacetime is very close to spherical symmetry and approximately stationary. We further investigate whether these small variations have any influence on the light rings' presence and structure. For this purpose we also display $\sigma(H_{\text{eff}})/\Delta H$ as the purple curve in Fig. S7, where ΔH is the potential difference between the extracted extrema of the AEP. Its value varies around $\sim 10^{-3} - 10^{-2}$, implying that the deviations from our symmetry assumptions explain at most 1% of the observed potential difference between the extrema.

The conclusions for **S06A044** are similar and displayed in Fig. S8. The major difference is that $\langle \beta^2 \rangle / \langle \alpha^2 \rangle \sim 10^{-6}$ is considerably larger now. This is in line with the

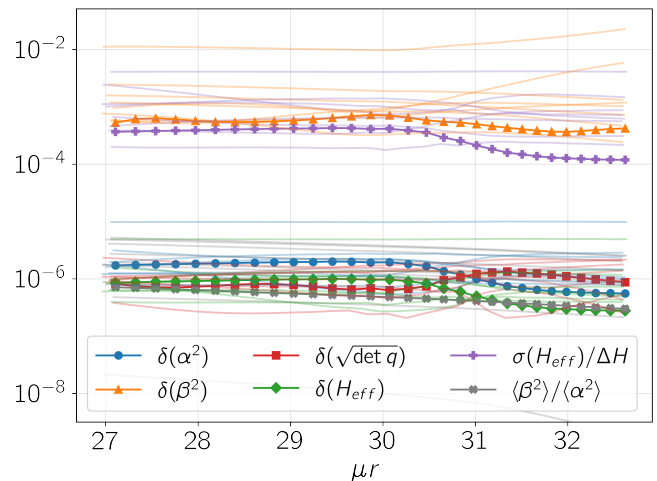


FIG. S8. Same as Fig. S7, but for BS model **S06A044**.

more pronounced oscillations also observed in other diagnostics for this numerically more challenging configuration; cf. Figs. 2 and 4 in the main text. The ratio $\sigma(H_{\text{eff}})/\Delta H \lesssim 10^{-3}$, however, is smaller by an order of magnitude, a side effect of the more pronounced extrema in the potential for this more extreme model.

V. RAY TRACING

The ray-traced images presented in this work (cf. Fig. 6 of the main text) are obtained using Flexible Object-Oriented Ray Tracer (FOORT), which is publicly available on GitHub [S5, S6]. The geodesic equations are integrated using the Runge-Kutta 4 or the Verlet scheme to produce images of a variety of spacetimes. FOORT is highly flexible and easily accommodates new analytical or numerical spacetimes. It employs adaptive mesh refinement (AMR) by refining the initially uniform grid in regions where selected image features change significantly.

The images in the main text are produced for the **S06A044** BS model using the Verlet scheme, for an observer located at areal radius $\mu r = 1000$ in units where the mass of the boson star is $\mu M \approx 10.4$. The image region has dimensions 150×150 in these units, and the highest resolution obtained with the AMR is ~ 0.047 . The insets focus on a region of 7.5×7.5 , with highest resolution ~ 0.0047 . The emission is modeled through an optically thin equatorial disk with emission profile given by [S7]

$$I_0(r) = [(r - \rho)^2 + \Delta^2]^{-1/2} \times \exp \left\{ -\frac{1}{2} \left[\kappa + \operatorname{arcsinh} \left(\frac{r - \rho}{\Delta} \right) \right]^2 \right\}. \quad (\text{S23})$$

The parameters used are $(\rho, \Delta, \kappa) = (60, 2.5, -2)$, with the first value corresponding to $\sim 6M$, the radial co-

ordinate of the ISCO in Schwarzschild spacetime. Although the spacetime is non-rotating, the fluid velocity can be modeled with a mix of radial and (sub)Keplerian orbits, as described in Refs. [S8, S9]. For the images

in the main text, parameters $\xi = \beta_r = \beta_\phi = 1.0$ (see Eqs. (B36), (B50), (B51) in Ref. [S9]) have been used, corresponding to pure Keplerian orbits which give rise to the observed asymmetry in the images.

-
- [S1] B. Kain, Boson stars and their radial oscillations, *Phys. Rev. D* **103**, 123003 (2021), arXiv:2106.01740 [gr-qc].
- [S2] M. Gleiser and R. Watkins, Gravitational Stability of Scalar Matter, *Nucl. Phys. B* **319**, 733 (1989).
- [S3] B.-X. Ge, E. A. Lim, U. Sperhake, T. Evstafyeva, D. Cors, E. de Jong, R. Croft, and T. Helfer, Hair is complicated: Gravitational waves from stable and unstable boson-star mergers, (2024), arXiv:2410.23839 [gr-qc].
- [S4] P. V. P. Cunha, C. Herdeiro, E. Radu, and N. Sanchis-Gual, Exotic Compact Objects and the Fate of the Light-Ring Instability, *Phys. Rev. Lett.* **130**, 061401 (2023), arXiv:2207.13713 [gr-qc].
- [S5] D. R. Mayerson, “FOORT: Flexible Object-Oriented Ray Tracing; <https://github.com/drmayerson/FOORT>,”
- [S6] D. R. Mayerson, F. Bacchini, and S. J. Staelens, FOORT: Flexible Object-Oriented Ray Tracing, (in prep.).
- [S7] S. E. Gralla, A. Lupsasca, and D. P. Marrone, The shape of the black hole photon ring: A precise test of strong-field general relativity, *Physical Review D* **102**, 124004 (2020).
- [S8] H.-Y. Pu, K. Akiyama, and K. Asada, The effects of accretion flow dynamics on the black hole shadow of Sagittarius A*, *The Astrophysical Journal* **831**, 4 (2016).
- [S9] A. Cárdenas-Avendaño, A. Lupsasca, and H. Zhu, Adaptive analytical ray tracing of black hole photon rings, *Phys. Rev. D* **107**, 043030 (2023).